

***Characterizing Lunar Ejecta Mobility in Rocky and
Non-Rocky Craters***

Brown University Independent Study Thesis

Tiffany Gao

2025

Mentored by Aleksandra Sokolowska

1. Abstract

Impact craters on the Moon are key features for understanding subsurface properties and impact dynamics. This report focuses on the analysis of cold-spot craters, a type of crater considered geologically young because their surrounding surfaces retain low-density fluffed-up material that has not yet compacted through space weathering processes. Using high-resolution imagery from the Lunar Reconnaissance Orbiter (LRO) and thermal data from the DIVINER instrument, we examine 50 cold-spot craters, comparing ejecta mobility between rocky and non-rocky craters. The findings show that craters excavating more consolidated material tend to have more constrained ejecta radii, while craters impacting unconsolidated regolith or loose materials produce broader ejecta blankets. This suggests a correlation between the scaled ejecta radius and rock abundance, with subsurface properties playing a significant role in determining the mobility and distribution of ejecta. While the degradation of surface features, reflectance properties of rocky and non-rocky ejecta components, and excavation process could complicate interpretation, we find that cold-spot craters help debunk these concerns. As a result, we conclude that variations in subsurface rheology are more likely responsible for influencing ejecta mobility.

2. Introduction

Impact craters are the most prominent geological features on planetary surfaces. They are formed when a hypervelocity meteorite hits a planetary surface, transferring its energy and momentum to the target, initiating the contact and compression, excavation, and modification stages of crater formation (Melosh, 1989). During the excavation stage, impact energy that isn't absorbed by the target surface transforms into kinetic energy that propels subsurface material outward to large distances in parabolic ballistic trajectories and partially mixes with the surface material upon landing, forming an ejecta blanket (Oberbeck, 1975).

Craters show a variety of geomorphological features that vary with their size, age, and the characteristics of the impacted surface, including its subsurface rheology. These features are not only shaped by the impact conditions but also by the mechanical properties of the target material. For instance, craters formed in layered subsurfaces, such as those with contrasting rheologies, often exhibit distinct morphologies (Prieur et al., 2018; Wood 1978). Flat-bottomed craters can form when the projectile excavates into a mechanically stronger layer beneath a weaker upper layer. Similarly, concentric craters may develop when subsurface layers with differing strengths deform unevenly during the impact process, resulting in ring-like structures. The presence of central peaks and terraced walls can reveal details about the properties of the target material (Prieur et al., 2018).

Ejecta blankets are particularly valuable geomorphological features to study as indicators of subsurface composition and structure. Fresh ejecta blankets, in particular, tend to be the most

prominent geomorphological features to study as they have ejecta that can fall to 5 radii from the center of the crater (French 1998). Young craters also show rays that form through the deposition of material from both the primary crater and secondary craters (Hawke 2004) which can fall up to 37 crater radii (Elliot 2018). The sizes of ejecta blankets and rays make them more easily identifiable in remote sensing data, such as high-resolution imagery from the Lunar Reconnaissance Orbiter Camera (LROC) (Chin 2007). Young craters, particularly those with well-preserved ejecta blankets and rays, provide a clearer view of impact dynamics, as these features degrade over time due to space weathering and micrometeorite bombardment (Denevi, 2023).

The characteristics of ejecta blankets are also influenced by the target's composition and mechanical properties (Barlow, 1990). For example, craters formed at low-impact angles often have asymmetrical ejecta blankets, with material deposited preferentially in the direction of impact (Anderson, 2006).

Rocky ejecta often indicates harder, more consolidated subsurface layers, while fine-grained ejecta suggest excavation of softer, unconsolidated materials (Horz et al., 1991). Studies used numerical simulations (Sokolowska et al. 2024a, 2024b) to study spatial distributions of ejecta blankets in relation to the subsurface rheology. These simulations show that in theory, spatial distributions of ejecta can vary and have the potential to become a new subsurface rheology diagnostic.

In particular, the so-called scaled ejecta radius (also known in literature as ejecta mobility, see e.g. Mouginis-Mark 1979) is a key parameter for studying ejecta. Scaled ejecta is defined as the radial distance of the outermost extent of ejecta deposits divided by the crater radius ($R_{\text{ejecta}} / R_{\text{crater}}$). Historically, this value has been assumed to be relatively constant, around 2–3 crater radii, with variations largely overlooked in many studies (Melosh, 1989). However, recent work challenges this assumption, showing that the scaled ejecta radius can vary significantly (Sokolowska et al. 2024a, 2024b). These variations are influenced, in part, by the subsurface rheology of the impacted material, suggesting that ejecta mobility could serve as a diagnostic tool for subsurface properties. However, the spatial scale at which these variations occur remains poorly understood, particularly on the Moon. Understanding these features is important because we know relatively little about the shallow subsurface of many planetary bodies. Upcoming space missions, such as those under the Artemis program (Smith et al., 2020), could benefit from a better understanding of its structure and mechanical properties.

Ejecta blankets are generally divided into two components: continuous ejecta, which typically extends 2–3 crater radii (2-3 R_{cr}) from the center, and discontinuous ejecta, which extend beyond 3 radii (3 R_{cr}) (French 1998; Melosh, 1989). Continuous ejecta blankets are

characterized by a relatively uniform thickness and surface morphology, while discontinuous ejecta exhibit patchy distributions and decreased thickness with distance.

Moreover, the constancy of the scaled ejecta radius also depends on the cratering regime—whether the crater formation is dominated by the material's strength or the gravitational forces. In the strength regime or at the transition to the gravity regime, deviations from the self-similar behavior of ejecta blankets are expected. Thus, one central question this thesis addresses is whether the scaled ejecta radius remains constant for craters of a given size.

One of the youngest crater types on the Moon for which we have high-resolution data of their ejecta are the so-called cold spot craters (Fig. 1). These craters are considered geologically young because their surrounding surfaces retain low-density, fluffed-up material that has not yet compacted through space weathering processes (Bandfield et al., 2014). When an impact occurs, it disturbs and heats the surface material, creating a distinctive thermal signature. Over time, this fluffed-up material merges with the surrounding background, but in cold spot craters, which are still geologically young, it appears thermally distinct, i.e. colder than the surrounding terrain. These signatures were observed by the Diviner instrument (Paige 2009) on the Lunar Reconnaissance Orbiter (Chin 2007).

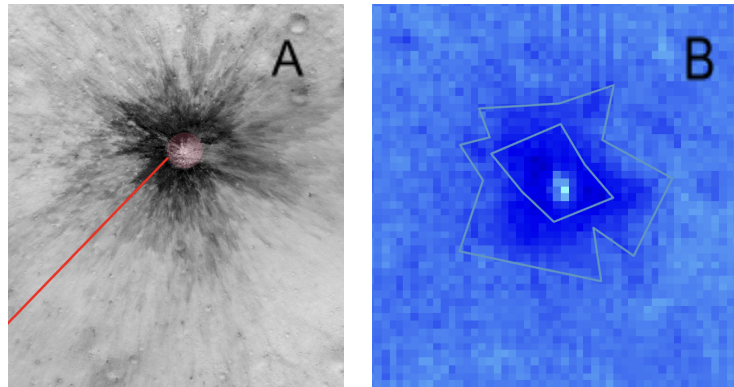


Fig. 1. An example of a cold spot is shown in (B) with Diviner H-Parameter data (Hayne et al., 2017) where dark blue is low thermal inertia and light blue is higher.

In this study, we analyze 50 cold spot craters to address key questions about the relationship between ejecta blanket characteristics and subsurface properties on the Moon. Specifically, we investigate 1) on what physical scale the scaled radius of ejecta blankets varies between objects, and 2) whether it correlates with rock abundance, providing insight into the mechanical properties of the impacted material. In order to answer the latter question, this

research seeks to compare the ejecta mobility between two distinct classes: rocky ejecta craters, which contain blocky, consolidated material, and non-rocky ejecta craters, characterized by unconsolidated, fine-grained material. Understanding these differences will provide valuable insights into how target material properties influence ejecta emplacement processes.

3. Methodology

3.1 Planetary data source

The Lunar Reconnaissance Orbiter (LRO) (Chin 2007) is a NASA mission launched in 2009 to map the Moon's surface. The LROC consisted of two types of imaging systems in its suite of instruments: the Wide Angle Camera (WAC) and the Narrow Angle Camera (NAC). The WAC provides lower-resolution images (approximately 100 meters per pixel) and a broader field of view while the NAC captures high-resolution images (approximately 0.5 meters per pixel), making it the most detailed imagery available for the Moon. The detail and resolution of the NAC images make it suited for studying fine-scale geomorphological features like ejecta blankets.

Another instrument aboard the LRO is the DIVINER Lunar Radiometer Experiment (Paige 2009). The DIVINER measures the thermal emission of the lunar surface to determine surface temperature, rock abundance, and other regolith properties.

A total of 314 cold-spot impact craters larger than 250 meters in diameter were identified by Williams et al. (2018) and their coordinates are publicly available.

3.2 Crater selection criteria

From this initial dataset of 314 craters, we selected 50 for detailed analysis. These craters were chosen based on four primary factors: (1) size, (2) rock abundance, (3) the incidence angle of available LROC NAC images, and (4) geographic distribution. The exact criteria are explained below.

We focused on a subset of 50 craters only to allow sufficient time for conducting detailed morphometric measurements of ejecta blankets during this semester-long independent study.

3.2.1 Crater Size

For our study, we focused on craters with diameters under 700 meters, specifically selecting those with diameters between 250 meters and 700 meters, for the following reason. Smaller craters than 700m require fewer NAC images for comprehensive analysis, making them more manageable within the time constraints of this study. Craters with diameters greater than 700 meters often require more images for accurate mapping of their ejecta blankets (with

blankets that can extend 5–6 radii from their center) significantly increasing the workload. By focusing on craters between 250 meters and 700 meters in diameter, we aim to strike a balance between obtaining sufficient data for analysis and managing the practical constraints of the study.

3.2.2 Rock Abundance

Rock abundance in the ejecta blankets of cold-spot craters was calculated using the Diviner rock abundance map (Paige 2009). Diviner's rock abundance estimates were derived from nighttime multispectral infrared observations (Bandfield et al., 2011). The fractional rock abundance (the fraction of the surface covered by coherent rocks) was then derived by using Diviner's data to measure the relative radiance contributions from the warmer rocks because rocks have higher thermal inertia than fine-grained regolith and remain warmer during the lunar night.

In this paper, when we refer to rock abundance, we are specifically discussing H_{Rock} , the "e-folding" depth. H_{Rock} is a parameter used to describe how the volume fraction of rocks increases with depth beneath the surface as calculated by Elder et al. (2019). This is important because, in impact craters, the excavation process moves subsurface material upward, and the deeper the excavation, the more likely it is that rocks from deeper layers are brought to the surface and included in the ejecta blanket.

The relationship between measured rock abundance (RA) and H_{Rock} is given by the following equation:

$$RA = \frac{\int_0^{d_e} (1 - e^{-z/H_{rock}}) dz}{d_e} = 1 - \frac{H_{rock}}{d_e} (1 - e^{-d_e/H_{rock}})$$

To address the central question of this thesis of whether ejecta radius differs with rock abundance we aim to select two contrasting populations of craters based on their rock abundance: high rock abundance and low rock abundance. To ensure a meaningful comparison, we divide the dataset into two groups based on the rock abundance threshold of 0.04–0.05, ensuring that approximately 50% of the craters fall below this threshold (low rock abundance) and 50% fall above it (high rock abundance). This allows us to analyze whether differences in rock abundance influence the ejecta radius. For a robust analysis, we also divided the dataset samples for very low rock abundance ($H_{Rock} < 0.02$) and very high rock abundance ($0.05 > H_{Rock} > 0.06$) leading to four distinct bins of craters divided by rock abundance. The four bins are ($H_{Rock} < 0.02$, $0.02 < H_{Rock} < 0.05$, $0.05 < H_{Rock} < 0.06$, $H_{Rock} > 0.07$) (Fig. 2B).

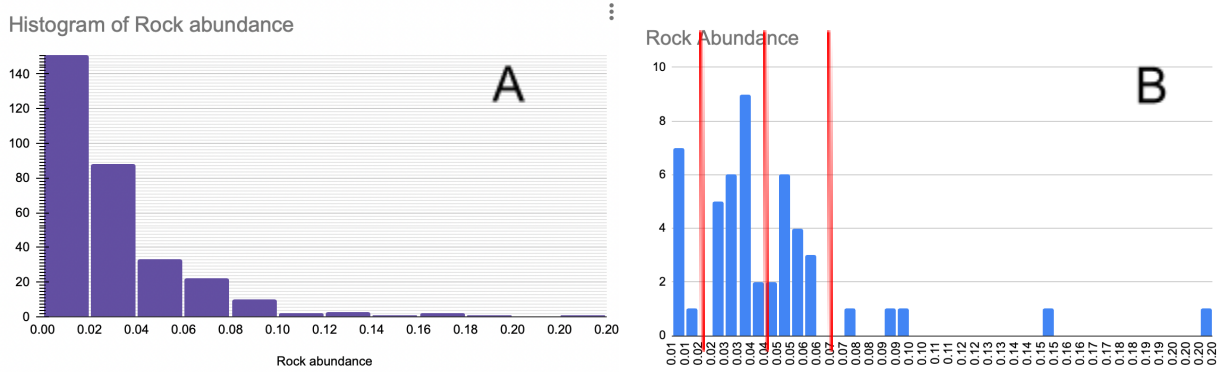


Fig. 2: (A) shows a histogram of all 314 craters organized by rock abundance into two bins. (B) shows a histogram of the 50 selected craters organized by rock abundance with red lines dividing them into 4 distinct bins.

3.2.3 Incidence Angle

The "angle of incidence" refers to the angle formed between a ray of sunlight striking a surface and the normal line that is perpendicular to that surface. Essentially it is the angle at which the sunlight is hitting the surface. An incidence angle of 0 means the sun is straight overhead (Fig. 3).

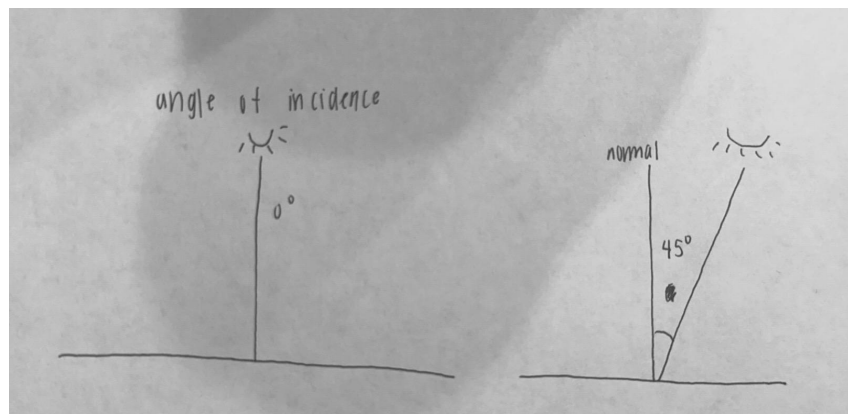


Fig. 3: An example of 0 degrees and 45 degrees angle of incidence.

A low incidence angle is generally preferred for observing prominent ejecta in LROC NAC images because lower incidence angles (less than 40°) provide better lighting conditions for distinguishing ejecta materials from the surrounding terrain. At higher incidence angles (~80°), the visibility of ejecta is significantly reduced because the surface is illuminated at a

steeper angle, causing shadows that obscure details of the ejecta blanket. The reduced contrast makes it difficult to differentiate the ejecta from the surrounding surface.

For our purposes, we limited the incidence angles of our NACs to 6-70 degrees. We tried to limit incidence angle as much as possible but limitations in NAC image availability sometimes necessitate the use of images with higher incidence angles.

3.2.4 Geographic Distribution

To probe diverse subsurface compositions and terrains, craters must span a wide range of latitudes and longitudes (Fig. 4). This ensures coverage of different geological settings, including basaltic mare regions and anorthositic highlands, enabling insights into variations in subsurface structures and materials across the Moon.

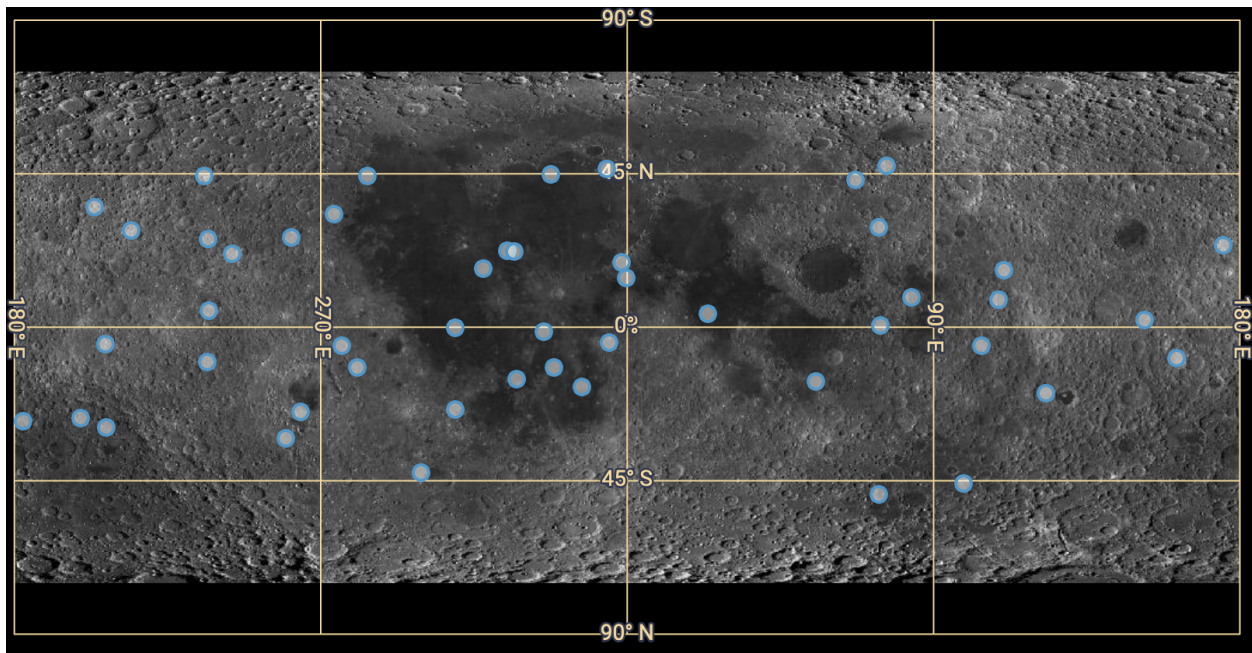


Fig. 4. Distribution of the 50 cold spot craters selected for analysis across different longitudes and latitudes.

3.3 Ejecta Mapping

3.3.1. Tools and Data Preparation

The ejecta of each cold spot crater was mapped in QGIS, an open-source Geographic Information System (GIS) software (Rosas-Chavoya, 2021), to outline distinct depositional layers based on observable changes in raster data. Raster data is spatial data represented by pixels, where grayscale pixel values represent the variations in surface reflectance or brightness, some of which can be attributed to ejecta on the surface (Fig. 5). We found that when the colormap/scale of the NAC image was inverted, we could better distinguish the boundaries of the ejecta deposit from the background surface. In such inverted images, darker pixels indicate lower

light reflectance which corresponds to thicker ejecta while lighter pixels represent thinner ejecta deposits.

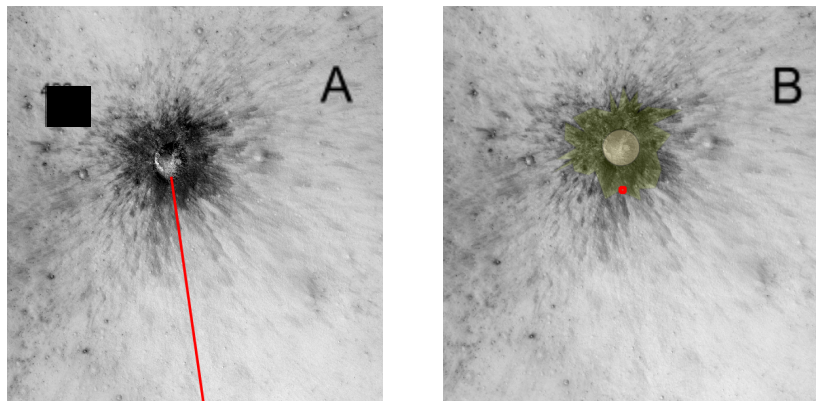
3.3.2 Identifying Ejecta Radius

Defining how to map the ejecta radius in the sample of our craters requires particular care because impact sites can vary in the scale of degradation. For this reason, we devised a new procedure that mitigates this issue.

Each cold spot crater was divided into several distinct morphological components: 1) a crater, 2) a continuous ejecta, and 3) three discontinuous ejecta levels. This departure from the traditional continuous/discontinuous, two-layer type of characterization is motivated by our observation of distinct levels of pixel intensity that are common amongst many objects in this sample. The maximal extents of these ejecta layers visible to the eye and later confirmed numerically were determined by analyzing changes in pixel intensity values along radial transects (a straight line drawn outward from the crater rim) using the Profile Tool plugin in QGIS (see Fig. 5A).

The Profile Tool plugin works by generating a radial profile of pixel intensity values (grayscale brightness) along the user-drawn line. The pixel intensity variation can be linked to changes in ejecta deposition and thickness. For the continuous ejecta layer and the first two discontinuous ejecta layers, distinct bumps followed by drops in the profile graph were used to define their boundaries (Fig. 5, levels B, C, D). Each bump in the graph represented a local increase in pixel intensity. The start of the bump marks a transition from thinner, more loosely packed ejecta to more densely packed deposits. The end of each bump results in a drop, where pixel values decreased significantly, which was interpreted as the end of the ejecta layer.

The third discontinuous ejecta layer was outlined primarily based on visual assessment in two-dimensional (2D) spatial data rather than on consistent measurable changes in the radial profile. This is because the ejecta material is discontinuous and patchy in nature, leading to variability in the pixel intensity values along radial profiles. When viewed in one-dimensional (1D) profiles, this patchiness manifests as noise, making it challenging to discern clear boundaries. However, when analyzing the ejecta in 2D, the spatial distribution of these discontinuous deposits becomes apparent, allowing for more reliable identification of the layer's extent based on its overall pattern and coverage.



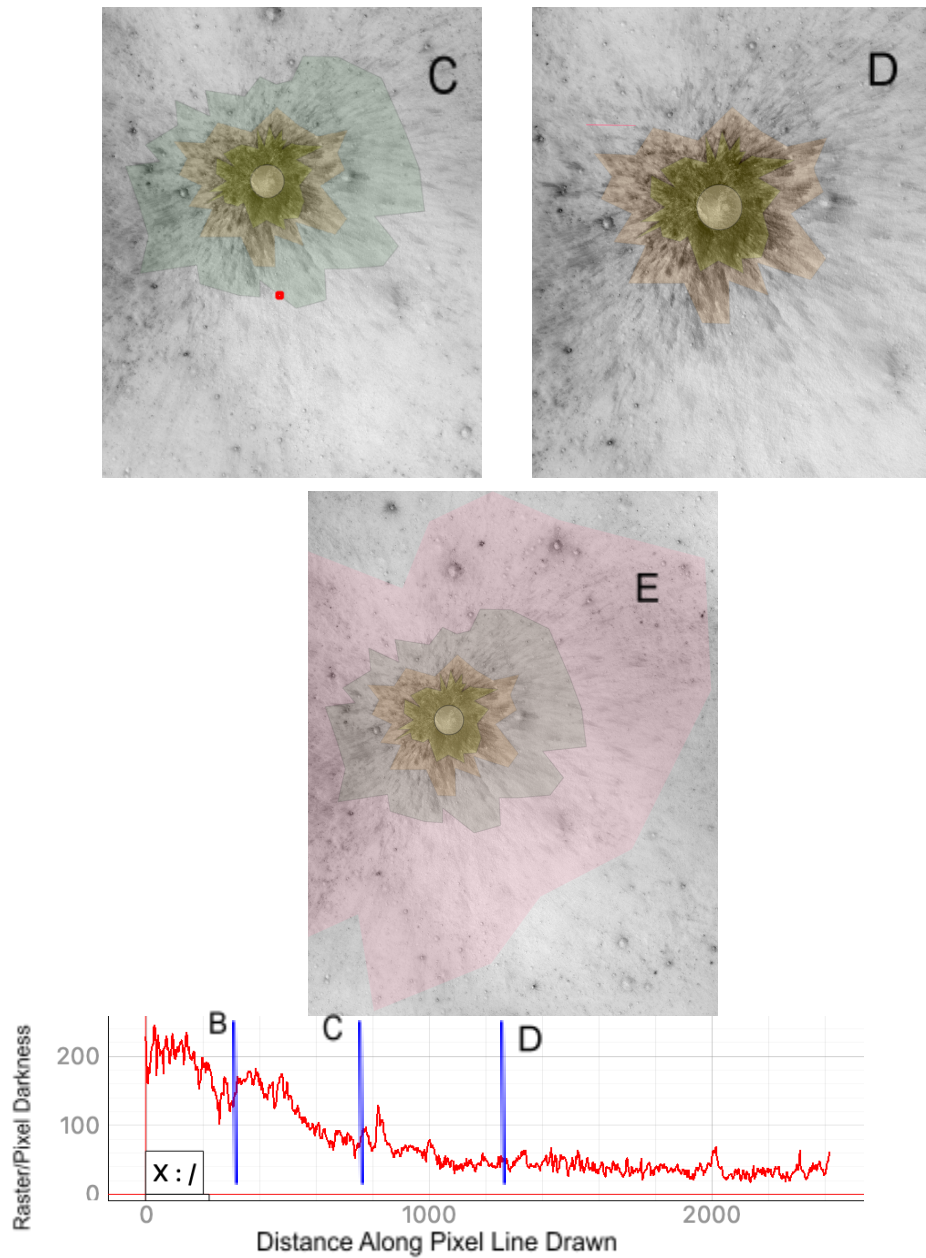
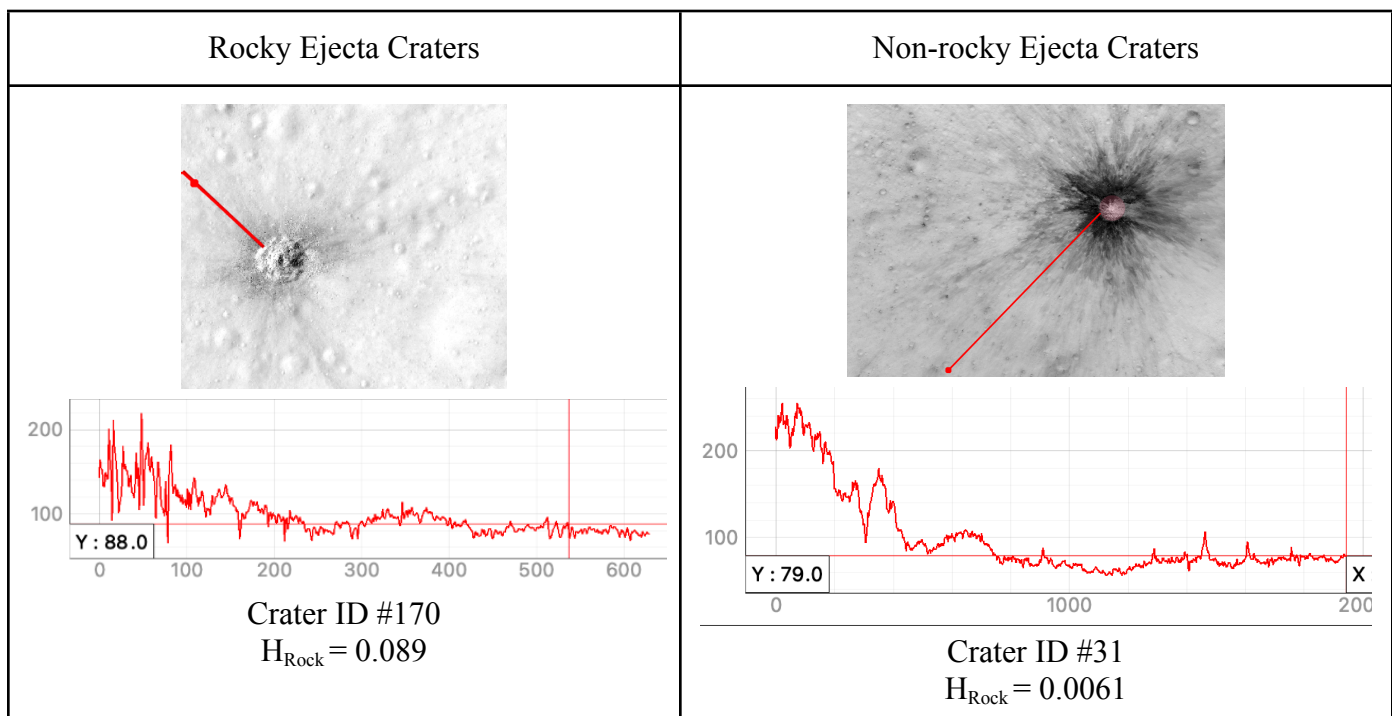


Fig. 5: Example of ejecta mapping using crater with ID #52 and LROC NAC image ID of M1237422334RC. (A) Shows the crater and ejecta with the pixel/raster darkness line drawn out from the crater. (B-D) Shows mapping of continuous ejecta and discontinuous ejecta 1 and 2 determined by distinct drops in pixel intensity values along the transect, corresponding to the respective letters and blue lines on the raster/pixel darkness graph. Figure E just shows the mapping of discontinuous ejecta 3 which is still visible to the naked eye but not on the graph.

3.3.3 Mapping with Lack of Ejecta Layers

The third discontinuous ejecta or the largest ejecta blanket could not be measured for seven craters due to time constraints and technical difficulties with converting NAC images to geotiffs. The lack of converted NAC images would affect the precision of the measurements leading to an underestimation of the true ejecta radii so we decided to omit them from analysis.

Additionally, when analyzing rocky craters with $H_{Rock} > 0.05$, some craters exhibit fewer distinct ejecta drops in the radial profiles of pixel intensity discussed above than the typical 3 bumps (Fig. 6). When this happens, ejecta mapping is simplified to include only two layers: a continuous ejecta layer and a third discontinuous ejecta layer. We chose to map it as the third discontinuous layer because they both display the same muddled and low pixel darkness between both rocky and nonrocky craters. This adjustment will reflect the reduced detectability of distinct ejecta drops and therefore the amount of ejecta layers in the raster profiles of rocky ejecta craters.



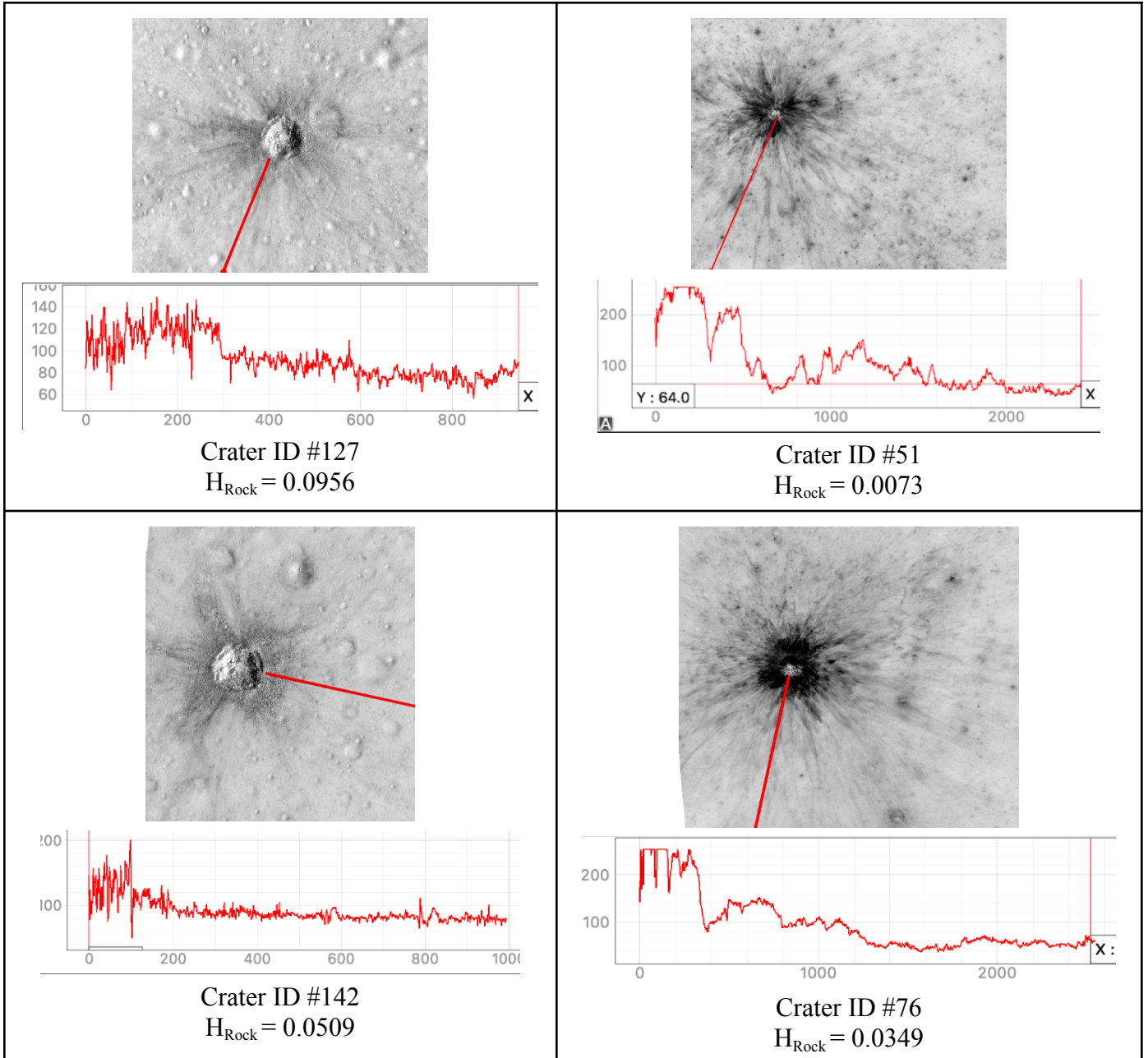


Fig. 6: 6 selected cold spot craters with their raster/pixel darkness graph and respective rockiness. Shows that the rockier craters have only two distinct drops while nonrocky craters have multiple.

4. Results

4.1 Calculating Ejecta Radii

To determine the radii of the ejecta blankets, we calculated the distances between the center of the crater and the boundaries of each mapped ejecta level. To do so, we first converted polygons which we drew for the ejecta levels in QGIS into line segments. Then we sampled those lines with equally spaced points placed every 50 meters and calculated the distance from each point to the crater's center.

To enable comparisons across craters of different sizes, we calculated the scaled ejecta radius for each ejecta layer. This was done by dividing the ejecta distances (R_{ejecta}) by the crater radius (R_{crater}), resulting in a dimensionless ratio (R_{ejecta} / R_{crater}). This approach allows for consistent analysis of ejecta distributions.

$$R_{scaled} = \frac{R_{ejecta}}{R_{crater}}$$

Using these distances, we calculated the median scaled ejecta radius for each crater. The median provides a robust measure of central tendency, reducing the impact of outliers or asymmetries in the ejecta blanket. This is because the simple average may not accurately represent the ejecta radius, especially in cases where the ejecta blanket is asymmetric or skewed to one side. In these cases, the average would be misleading.

We also calculated the median absolute deviation (MAD) to assess the variability in ejecta distances. This statistic measures the spread of distances around the median. The calculation for MAD is given by the equation below:

$$MAD(R_{scaled}) = Median(|R_{scaled} - Median(R_{scaled})|)$$

The median and MAD provide a statistically sound framework for analyzing ejecta radii, accounting for central tendency and variability.

4.2 The Scale of Variations in Ejecta Radii

To further assess the scale of variation in ejecta radii, we plotted histograms of the medians of all craters for each ejecta layer. These histograms help us visualize the distribution of

scaled ejecta radii across different craters, offering insight into how typical ejecta radii vary for each layer and whether any craters deviate significantly from the central trend (Fig. 7).

For the 50 cold spot craters analyzed for the continuous ejecta, the median scaled ejecta radius was 1.487, with a median absolute deviation (MAD) of 0.178. This indicates that most of the ejecta radii are clustered around this central value of 1.487, but there is notable variability. The minimum scaled ejecta radius measured 0.854, while the maximum value reached 2.313, resulting in a delta (range) of 1.459 (Table. 1).

As the ejecta levels increase from continuous ejecta to the outermost discontinuous ejecta, the median scaled ejecta radius increases consistently. For layer 2, the median scaled ejecta radius is 2.426 and for layers 3 and 4 it is 3.777 and 6.506 respectively. This increase reflects the extended trend that higher ejecta layers extend further from the crater rim. The delta (range) for layer 4 (13.199) is an order of magnitude than the range for layer 1 which shows that there is more variability for the outermost layers as the variability increases with each layer.

These findings show a clear relationship between ejecta layer level and radial extent, with increasing ejecta layer level corresponding to greater scaled radii.

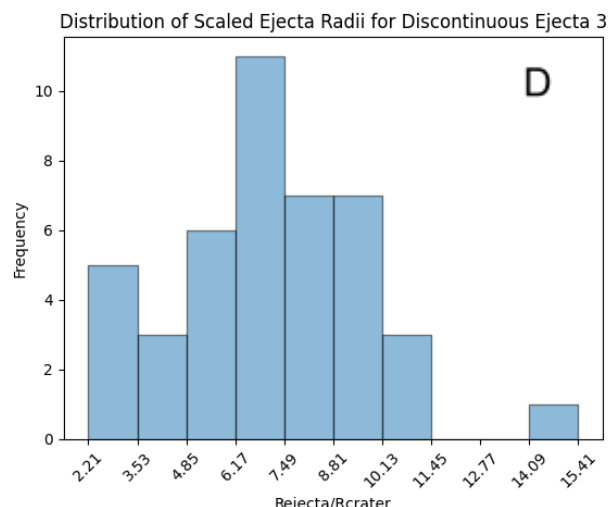
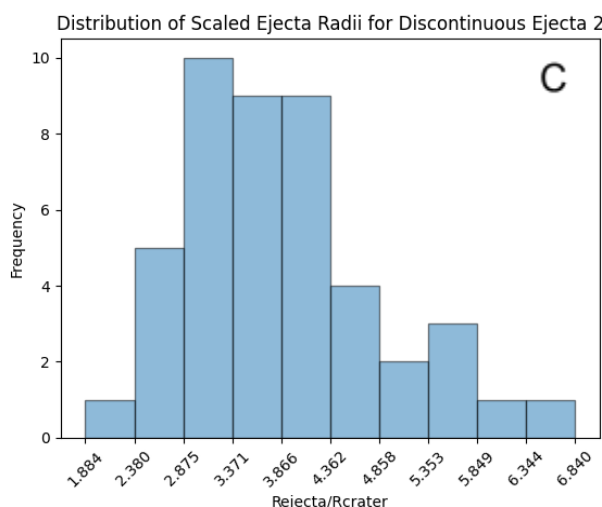
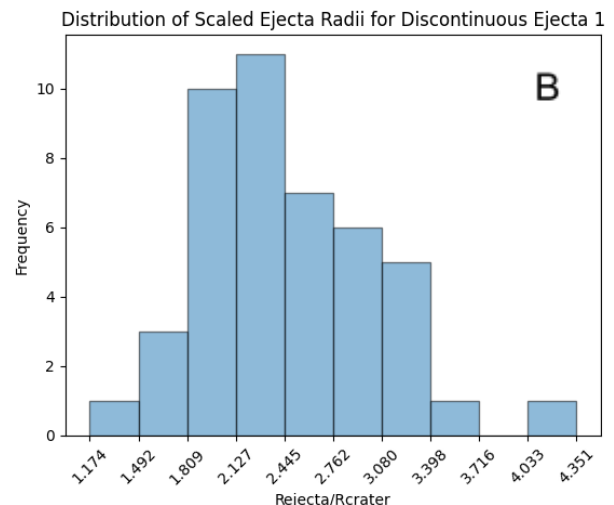
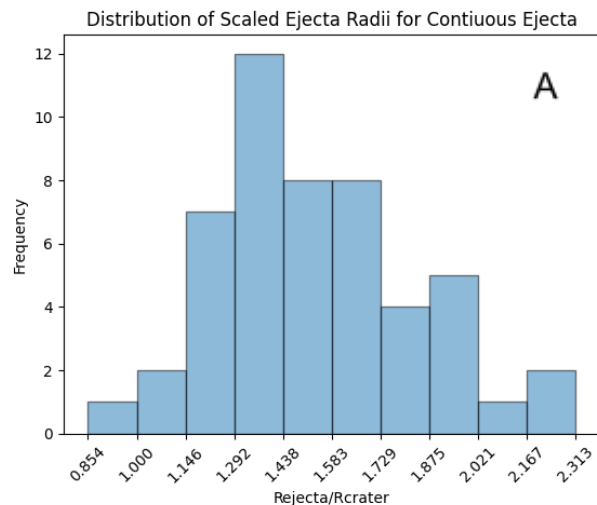


Fig. 7: Histograms of the distribution of scaled ejecta radii across four ejecta layers with 10 bins. (A) Continuous Ejecta between a scaled ejecta radius of 0.854 and 2.313 (B) Discontinuous Ejecta 1 between a scaled ejecta radius of 1.174 and 4.351 (C) Ejecta Layer 3: Discontinuous Ejecta 2 between a scaled ejecta radius of 1.884 and 6.840 (D) Ejecta Layer 4: Discontinuous Ejecta 3 between a scaled ejecta radius of 2.21 and 15.41.

Ejecta Level	Median (R _{scaled})	MAD (R _{scaled})	Min (R _{scaled})	Max (R _{scaled})	DELTA (R _{scaled})	DELTA * 500m
1 (continuous)	1.487	0.178	0.854	2.313	1.459	729.5m
2 (discontinuous 1)	2.426	0.418	1.174	4.351	3.177	1588.5m
3 (discontinuous 2)	3.777	0.662	1.884	6.84	4.956	2478m
4 (discontinuous 3)	6.506	1.907	2.208	15.407	13.199	6599.5m

Table 1: Summary of Scaled Ejecta Radii Statistics for Each Ejecta Layer. The table shows the median scaled ejecta radii (Rscaled), median absolute deviation (MAD), minimum and maximum Rscaled, and delta (range) for continuous ejecta (layer 1) and three discontinuous ejecta layers (layers 2–4). Outer layers exhibit greater radii and variability, with delta values growing from 729.5 m (layer 1) to 6599.5 m (layer 4), reflecting broader material dispersion at higher layers.

The clear stratification of ejecta radii across these layers suggests that different subsurface properties, such as material strength, composition, or structural integrity, may influence the way the material is ejected and distributed. The ejecta exhibit greater radial extends and become more discontinuous, this indicates that deeper layers within the lunar target may play a big role in determining how the material is displaced during impact events.

4.3 Rocky/Non-Rocky Ejecta Radii

To analyze if the ejecta associated with rocky and nonrocky craters show notable differences in their distributions, we plotted histograms of the rocky and nonrocky distributions on the same histogram allowing us to visualize if there are noticeable differences between the distribution of scaled ejecta radii between the two groups (Fig. 8).

Nonrocky ejecta generally extend farther from the impact site compared to rocky ejecta for all layers with the nonrocky materials extending even farther for higher levels. For level 1, the distribution of non-rocky ejecta is centered around a Rejecta/Rcrater ratio of 1.4–1.5, with a

median radius of 1.59 ± 0.197 . As we move to higher levels, the radii for non-rocky ejecta continue to show a broader spread, peaking at 2.2–2.5 for level 2 (median radius 2.434 ± 0.339), 3.7–4.3 for level 3 (median radius 3.828 ± 0.484), and 5.6–6.4 and 7.8–8.5 for level 4 (median radius 6.875 ± 1.380). This shows that nonrocky materials are ejected further from the crater likely due to their lower mass which allows them to travel greater distances. In contrast, rocky ejecta exhibit a more compact distribution with radii that are smaller and more concentrated towards the crater and impact site (Table 2).

The histograms for rocky ejecta are characterized by a right-skewed distribution, particularly at higher ejecta levels. For level 1, the peak is around a Rejecta/Rcrater ratio of 1.3–1.6 (median radius 1.398 ± 0.156). At higher levels, the radii show less spread compared to the non-rocky ejecta, with rocky ejecta at level 2 centered around a Rejecta/Rcrater ratio of 1.8–2.3 (median radius 1.969 ± 0.356), level 3 at 2.5–3.0 (median radius 3.025 ± 3.025), and level 4 at 2.9–4.3 (median radius 3.995 ± 1.574). These trends are likely due to the presence of larger, denser boulders that are deposited closer to the crater resulting in smaller radii for the ejecta patterns.

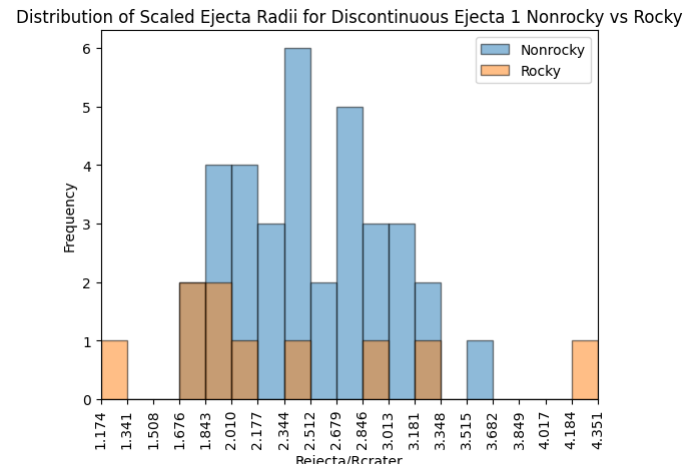
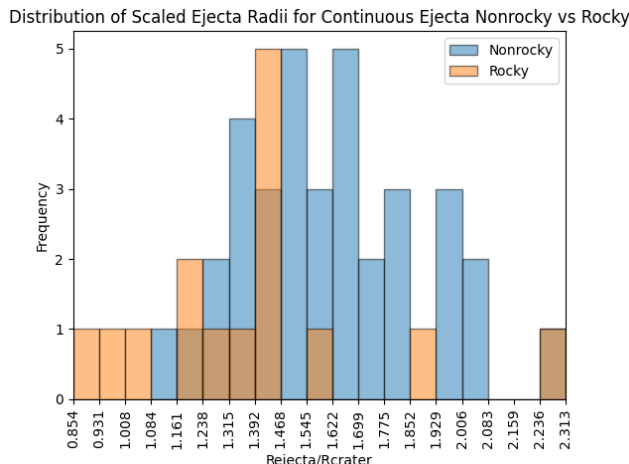
The maximum/radial extent of the boulder field of rocky craters is discontinuous ejecta layer 2. While boulders are commonly found in the first two discontinuous layers, they are rarely observed in the third discontinuous layer. This suggests that rocky ejecta primarily settles within the first two layers, with the majority of larger boulders being deposited relatively close to the crater. In contrast, non-rocky ejecta, which is composed of finer, lighter materials, tends to extend further outward, as evidenced by the broader radii distributions observed at higher ejecta levels.

Although there is substantial overlap in the histogram radii distributions between rocky and nonrocky ejecta in the lower levels, the differences are more pronounced at higher levels. For discontinuous ejecta 2 and 3, the distribution for rocky ejecta is right-skewed, suggesting a more concentrated deposition of larger fragments, while non-rocky ejecta continues to show a broader spread. These findings confirm that rocky ejecta tend to extend less far than non-rocky ejecta.

Ejecta Level	Non-Rocky Ejecta (Median (R_{scaled}) \pm MAD)	Rocky Ejecta (Median (R_{scaled}) \pm MAD)	Shape of histograms
1 (continuous)	1.59 ± 0.197	1.398 ± 0.156	Nonrocky crater distribution is roughly symmetric. Peak at Rejecta/Rcrater 1.4–1.5. Rocky craters have a peak

			around of 1.3-1.6.
2 (discontinuous 1)	2.434 ± 0.339	1.969 ± 0.356	Distribution for nonrocky has a peak around Rejecta/Rcrater 2.2–2.5. Rocky crater distribution is more sparse with a broader spread.
3 (discontinuous 2)	3.828 ± 0.484	3.025 ± 3.025	The nonrocky craters distribution shows a peak around Rejecta/Rcrater 3.7–4.3. Rocky crater distribution is sparse and has isolated counts at higher values.
4 (discontinuous 3)	6.875 ± 1.380	3.995 ± 1.574	Nonrocky has a little bimodal-like distribution with peaks at Rejecta/Rcrater 5.6–6.4 and 7.8–8.5. Rocky craters distribution is right skewed with most frequencies concentrated at Rejecta/Rcrater 2.9–4.3.

Table 2: Comparison of Scaled Ejecta Radii for Non-Rocky and Rocky Ejecta. Median scaled ejecta radii (R_{scaled}) and their variability ($\pm MAD$) are shown for non-rocky and rocky ejecta across all layers. Non-rocky ejecta consistently exhibit larger radii and greater variability compared to rocky ejecta, with differences becoming more pronounced at higher ejecta levels



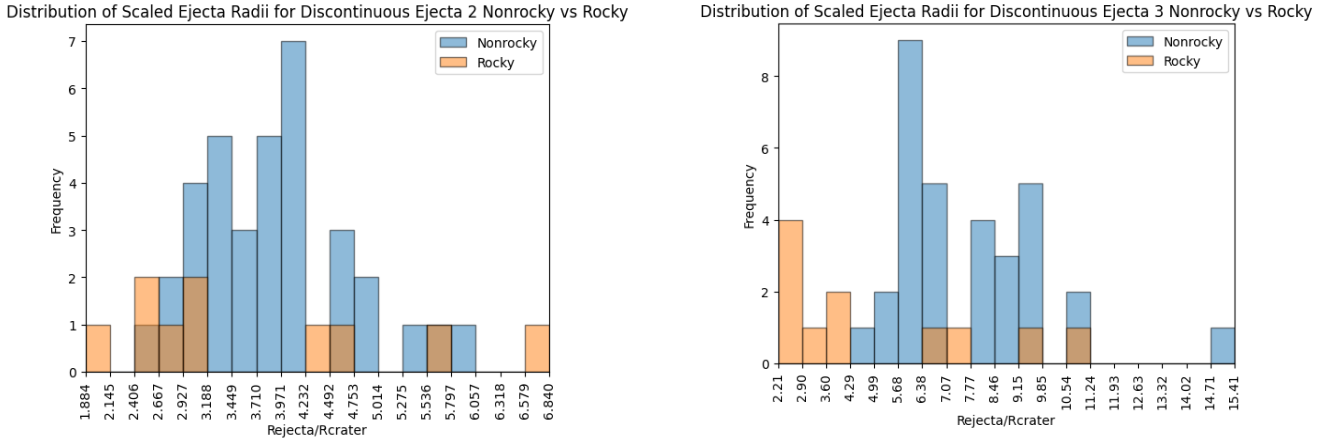


Fig. 8: Histograms of the distribution of scaled ejecta radii across four ejecta layers comparing nonrocky to rocky ejecta

5. Discussion

In the study, we observed that craters excavating more consolidated material tend to have more constrained ejecta radii, while craters impacting unconsolidated regolith or other loose materials produce broader ejecta blankets. This suggests a correlation between the scaled ejecta radius and rock abundance, suggesting that subsurface properties play a significant role in determining the mobility and distribution of ejecta. However, the interpretation of these results is not straightforward due to several complicating factors: (1) the surface features of impact sites vary in terms of degradation, (2) rocky and non-rocky ejecta components exhibit different reflectance properties, and (3) the excavation process depends on the number, order, and thickness of subsurface layers, as demonstrated by Sokolowska et al. (2024). We do believe that these are nonissues as we would explain below as the degradation and reflectance properties are usually debunked by the cold spot craters.

5.1 Subsurface Rheology and Excavation

The lunar subsurface is typically composed of a layer of regolith, which is unconsolidated and weak, overlying a bedrock layer that is more consolidated and stronger. (Venkatraman 2023) The thickness of the regolith layer can vary depending on the location on the Moon (e.g., mare versus highlands regions), as well as the degree of impact gardening, the process by which previous impacts alter the structure and composition of the regolith.

When an impact event occurs, the depth to which the impact penetrates can determine the type of material excavated and, therefore, the nature of the ejecta. For instance, impacts that penetrate deeply into the regolith layer may excavate both regolith and underlying bedrock which will result in a mixture of rocky ejecta and unconsolidated material. The deeper the impact penetrates, the more likely it is that material from the bedrock layer is excavated and incorporated into the ejecta. This explains why rocky ejecta is often concentrated within the continuous and first two discontinuous layers, while non-rocky ejecta can extend farther. A high-energy impact may penetrate deeper, excavating both regolith and bedrock while low-energy impacts only disturb the upper regolith layers resulting in ejecta consisting primarily of fine-grained, unconsolidated material.

5.2 Boulder Field Ejecta

Boulder fields in impact cratering often mark the extent of ejecta, with larger rocks and boulders providing a distinct boundary for the ejected material. However, when these boulders are not visible or are absent throughout the ejecta (like in our data where the boulders are not visible in discontinuous ejecta 3), this could suggest that the ejecta has already undergone significant weathering and erosion. The absence of boulders, or the indistinguishability of ejecta from the background regolith, could indicate that the material has been weathered away, potentially due to the age of the crater or ongoing processes like impact gardening.

At this stage, it's challenging to definitively determine whether the absence of boulders is due to erosion or other factors such as impact energy or subsurface material properties. While erosion might explain the disappearance of boulders in older craters, the impact's energy and depth of excavation also play a role.

While it is difficult to conclude definitively with the data currently at hand, analyzing the cold spot temperature offers because it allows us to compare the ages between craters. The presence of cold spots, or lack thereof, can provide a clear indication of crater age and the degree to which surface features, including boulders, have been weathered. I will explore this in more detail in the next section.

5.3 Influence of Crater Age and Degradation

It is important to note that as stated before, crater age and surface degradation can complicate the interpretation of ejecta features. One hypothesis for this pattern is that it is not a consequence of the rockiness of the subsurface material but rather that the rocky craters selected for mapping are older cold spot craters where ejecta features have been eroded or degraded over time. Such erosion would have led to the reduced number of detectable ejecta layers in the raster graph and the lighter color of the ejecta in the NAC images.

To determine if the raster data was affected by the age of the regolith (or the degradation amount), we compared the Regolith Temperature Anomaly using data from the Lunar Reconnaissance Orbiter (LRO) DIVINER instrument.

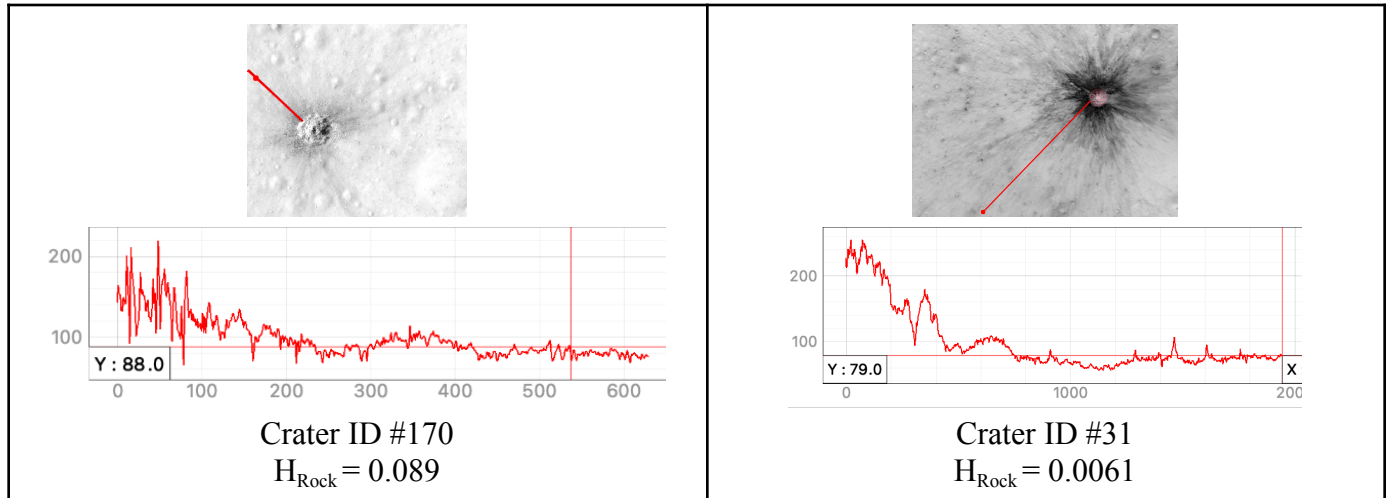
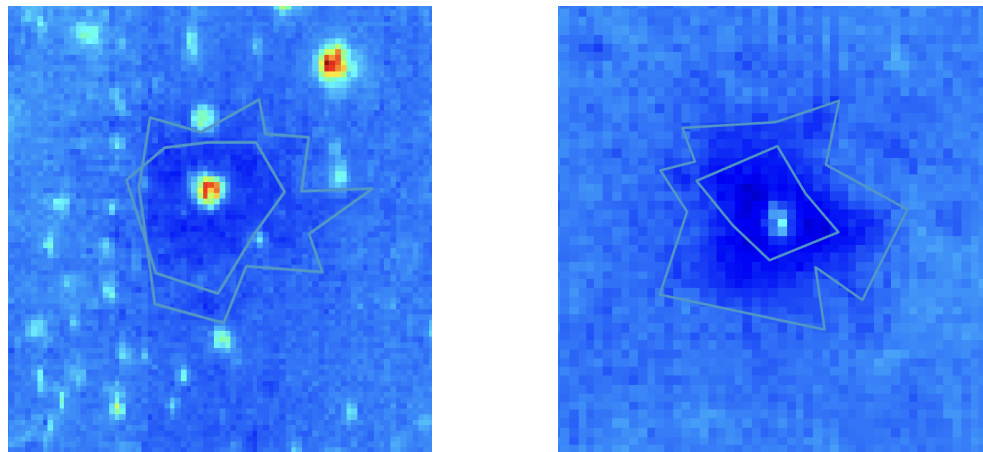


Fig. 9: Crater #170 and Crater #31, two cold spot craters with their raster/pixel darkness graph and respective rockiness. They have completely different raster/pixel graphs and different spreads of ejecta.

Both rocky crater #170 and nonrocky crater #31 exhibit similarly low Regolith Temperature Anomaly values even though #170 appears more “weathered” (Fig. 9), indicating that they are both relatively cold and young. This suggests that the crater Crater #170 is not significantly younger than Crater #31. Therefore the difference in pixel darkness and the number of detectable ejecta layers are more likely attributed to variations in subsurface rheology rather than due to age and erosion (Fig. 10).



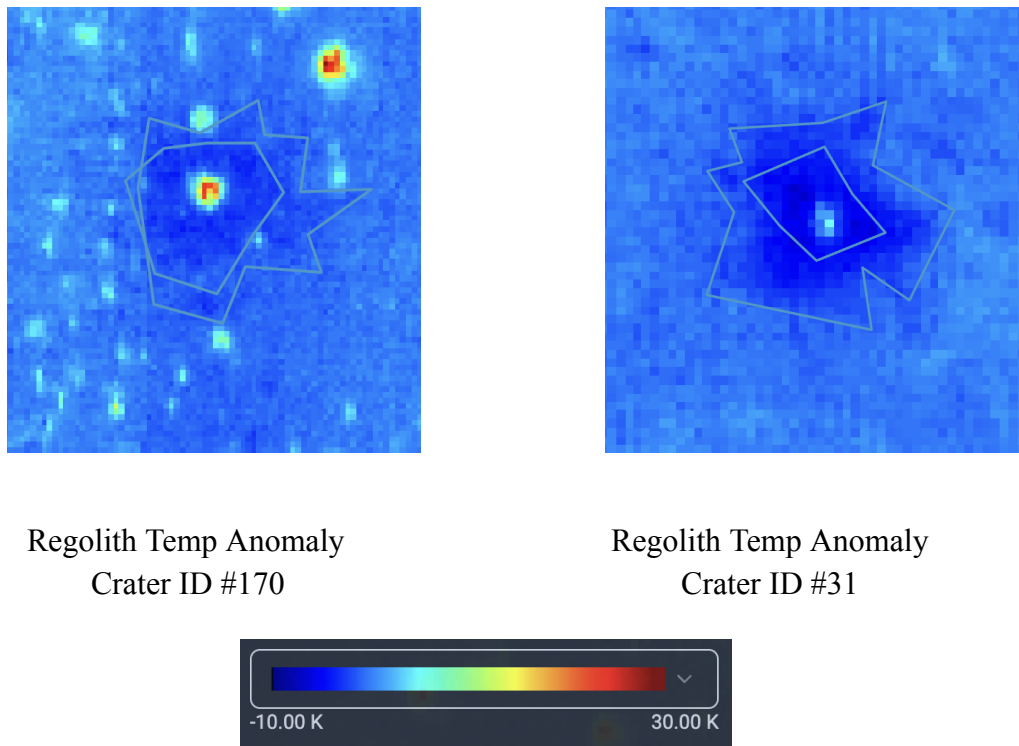


Fig. 10: An example of a cold spot shown in (B) Diviner H-Parameter data (Hayne et al., 2017) where dark blue is low thermal inertia and light blue is higher. This shows that both Crater #170 and Crater #31 have similar temperature signatures despite different rock abundance showing similar ages.

This finding challenges the notion that crater age and erosion are significant factors in explaining the differences in pixel darkness and the number of detectable ejecta layers. Instead, these differences are more likely attributed to variations in subsurface rheology, as previously discussed.

6. Future Work and Conclusion

In this report, we explore the hypothesis that variations in the spatial distribution of ejecta blankets observed on the Moon are influenced by subsurface rheology. However, further work is necessary to refine and expand on these findings. Future studies could benefit from a broader sampling of cold-spot craters and more time to adequately process all the images for analysis. Additionally, incorporating data from other instruments could provide more detailed topographic information and a more accurate measure of where the boulder field extent lies.

Another approach could involve mapping the ejecta based on the boulder field extent, excluding regions with no boulders from the calculations, to focus on areas that are most representative of the subsurface rheology influence.

In conclusion, this study provides strong evidence that variations in subsurface rheology are the primary driver of differences in ejecta mobility between rocky and non-rocky craters but further analyses are still necessary to fully constrain this hypothesis.

7. References

- French, B. M. (1998). *Traces of Catastrophe*.
- Melosh, H. J. (1989). *Impact Cratering*. Oxford University Press, USA.
- Oberbeck, V. R. (1975). The role of ballistic erosion and sedimentation in lunar stratigraphy. *Reviews of Geophysics*, 13(2), 337. <https://doi.org/10.1029/rg013i002p00337>
- Prieur, N. C., Rolf, T., Wünnemann, K., & Werner, S. C. (2018). Formation of Simple Impact Craters in Layered Targets: Implications for Lunar Crater Morphology and Regolith Thickness. *Journal of Geophysical Research: Planets*, 123(6), 1555–1578. <https://doi.org/10.1029/2017je005463>
- Anderson, J. L. B., & Schultz, P. H. (2006). Flow-field center migration during vertical and oblique impacts. *International Journal of Impact Engineering*, 33(1-12), 35–44. <https://doi.org/10.1016/j.ijimpeng.2006.09.022>
- Williams, J. -P, Bandfield, J. L., Paige, D. A., Powell, T. M., Greenhagen, B. T., Taylor, S., Hayne, P. O., Speyerer, E. J., Ghent, R. R., & Costello, E. S. (2018). Lunar Cold Spots and Crater Production on the Moon. *Journal of Geophysical Research Planets*, 123(9), 2380–2392. <https://doi.org/10.1029/2018je005652>
- Bandfield, J. L., Ghent, R. R., Vasavada, A. R., Paige, D. A., Lawrence, S. J., & Robinson, M. S. (2011). Lunar surface rock abundance and regolith fines temperatures derived from LRO Diviner Radiometer data. *Journal of Geophysical Research*, 116. <https://doi.org/10.1029/2011je003866>
- Elder, C. M., Douglass, B., Ghent, R. R., Hayne, P. O., Williams, J.-P., Bandfield, J. L., & Costello, E. (2019). The Subsurface Coherent Rock Content of the Moon as Revealed by Cold-Spot Craters. *Journal of Geophysical Research. Planets*, 124(12), 3373–3384. <https://doi.org/10.1029/2019je006128>
- Paige, D. A., Foote, M. C., Greenhagen, B. T., Schofield, J. T., Calcutt, S., Vasavada, A. R., Preston, D. J., Taylor, F. W., Allen, C. C., Snook, K. J., Jakosky, B. M., Murray, B. C., Soderblom, L. A., Jau, B., Loring, S., Bulharowski, J., Bowles, N. E., Thomas, I. R., Sullivan, M. T., & Avis, C. (2009). The Lunar Reconnaissance Orbiter Diviner Lunar Radiometer Experiment. *Space Science Reviews*, 150(1-4), 125–160. <https://doi.org/10.1007/s11214-009-9529-2>

- Chin, G., Brylow, S., Foote, M., Garvin, J., Kasper, J., Keller, J., Litvak, M., Mitrofanov, I., Paige, D., Raney, K., Robinson, M., Sanin, A., Smith, D., Spence, H., Spudis, P., Stern, S. A., & Zuber, M. (2007). Lunar Reconnaissance Orbiter Overview: The Instrument Suite and Mission. *Space Science Reviews*, 129(4), 391–419.
<https://doi.org/10.1007/s11214-007-9153-y>
- Barlow, N. G., & Bradley, T. L. (1990). Martian impact craters: Correlations of ejecta and interior morphologies with diameter, latitude, and terrain. *Icarus*, 87(1), 156–179.
[https://doi.org/10.1016/0019-1035\(90\)90026-6](https://doi.org/10.1016/0019-1035(90)90026-6)
- Wood, (2025). Interior morphology of fresh martian craters: The effects of target characteristics. *Lunar and Planetary Science Conference Proceedings*, 3, 3691–3709.
<https://ui.adsabs.harvard.edu/abs/1978LPSC....9.3691W/abstract>
- Mouginis-Mark, P. (1979). Martian fluidized crater morphology: Variations with crater size, latitude, altitude, and target material. *Journal of Geophysical Research*, 84(B14), 8011.
<https://doi.org/10.1029/jb084ib14p08011>
- Elliott, J. R., Huang, Y.-H., Minton, D. A., & Freed, A. M. (2018). The length of lunar crater rays explained using secondary crater scaling. *Icarus*, 312, 231–246.
<https://doi.org/10.1016/j.icarus.2018.04.015>
- Hawke, B. Ray., Blewett, D. T., Lucey, P. G., Smith, G. A., Bell, J. F., Campbell, B. A., & Robinson, M. S. (2004). The origin of lunar crater rays. *Icarus*, 170(1), 1–16.
<https://doi.org/10.1016/j.icarus.2004.02.013>
- Denevi, B. W., Noble, S. K., Christoffersen, R., Thompson, M. S., Glotch, T. D., Blewett, D. T., Garrick-Bethell, I., Gillis-Davis, J. J., Greenhagen, B. T., Hendrix, A. R., Hurley, D. M., Keller, L. P., Kramer, G. Y., & Trang, D. (2023). Space Weathering At The Moon. *Reviews in Mineralogy and Geochemistry*, 89(1), 611–650.
<https://doi.org/10.2138/rmg.2023.89.14>
- Bandfield, J. L., Song, E., Hayne, P. O., Brand, B. D., Ghent, R. R., Vasavada, A. R., & Paige, D. A. (2014). Lunar cold spots: Granular flow features and extensive insulating materials surrounding young craters. *Icarus*, 231, 221–231.
<https://doi.org/10.1016/j.icarus.2013.12.017>
- Venkatraman, J., Horvath, T., Powell, T. M., & Paige, D. A. (2023). Statistical estimates of rock-free lunar regolith thickness from diviner. *Planetary and Space Science*, 229, 105662. <https://doi.org/10.1016/j.pss.2023.105662>
- Rosas-Chavoya, M., Gallardo-Salazar, J. L., López-Serrano, P. M., Alcántara-Concepción, P. C., & León-Miranda, A. K. (2022). QGIS a constantly growing free and open-source geospatial software contributing to scientific development. *Cuadernos de Investigación Geográfica*, 48(1), 197–213. <https://doi.org/10.18172/cig.5143>
- Hörz, F., Grieve, R., Heiken, G., Spudis, P., & Binder, A. (1991). Lunar Surface Processes. In NASA ADS. <https://ui.adsabs.harvard.edu/abs/1991lsug.book...61H/abstract>

- Sokołowska, A., Thomas, N., & Wünnemann, K. (2024). Effects of surface and subsurface water/ice on spatial distributions of impact crater ejecta on Mars. *Icarus*, 420, 116150. <https://doi.org/10.1016/j.icarus.2024.116150>
- Smith, M., Craig, D., Herrmann, N., Mahoney, E., Krezel, J., McIntyre, N., & Goodliff, K. (2020, March 1). The Artemis Program: An Overview of NASA's Activities to Return Humans to the Moon. IEEE Xplore. <https://doi.org/10.1109/AERO47225.2020.9172323>